An Analysis of SkySat-1 Attitude Determination and Control

Christopher Covert

Revision History

Table 1: Report Changelog

Rev	Changes
PS1	- Created document
	- Added PS1 material
PS2	- Added PS2 material
	- Revised typos from PS1
PS3	- Added PS3 material
PS4	- Added PS4 material
PS5	- Added PS5 material
PS6	- Added PS6 material
FINAL	- Added UKF Estimation Results
	- Reorganized Sections
	- Updated graphs to reflect new covariances
	- Adding pointing error plot from PS2
	- Changed angular velocity plot to angular momentum from PS5
	- Added conclusions/future work section

Contents

List of Figures

List of Tables

1 Background

SkySat-1 and SkySat-2 are microsatellites built and operated by Skybox Imaging that acquire high resolution panchromatic and multispectral images of Earth. The spacecraft are three-axis stabilized by using an on-board closed-loop control system without any propulsion. Each satellite has a mass of 83 kg and features body-mounted solar panels. The microsatellites also feature an aperture cover that protects the imaging payload during launch and initial orbital operations. The cover also hosts the high-data rate antenna of the satellite.[30]

By April 2012, Skybox Imaging (Mountain View, CA) had raised a total of $91 million of private capital from Khosla Ventures, Bessemer Venture Partners, Canaan Partners and Norwest Venture Partners to develop the SkySat constellation.[5]

On November 21, 2013, the first satellite, SkySat-1, was launched on a Dnepr rocket from Yasny, Russia.[13]

On June 10, 2014, Skybox Imaging announced that it had entered into an agreement to be acquired by Google for $500 million.[23][24] Skybox Imaging changed its name to "Terra Bella" on March 8, 2016, to indicate its focus on image analytics.[25] The new name was partially based on the Terra Bella Ave. in Mountain View, California, where the company's headquarters are located.[26]

In 2017, Google sold Terra Bella and its SkySat satellite constellation to Planet Labs for an undisclosed price and entered into a multi-year agreement to purchase SkySat imaging data.[28]

2 Mission Description and Requirements

2.1 Mission Objectives

The resolution of the SkySat satellite imagery and videos is high enough to observe objects that impact the global economy such as terrain, cars and shipping containers. The satellites can capture video clips lasting up to 90 seconds at 30 frames per second.[5] The high-definition satellite video from SkySat satellites is aimed to help understand the world better by analyzing movement of goods and people, providing visual data about supply chains, shipping, industrial plant activity, and even humanitarian relief efforts. [4]

The constellation's goal is to be able to provide high-resolution satellite imagery of any place on Earth multiple times a day. [5] When Skybox originally developed the satellites, they planned to change the nature of the satellite industry by building satellites with off-the-shelf electronics that cost under $50 million. [5]

2.2   Spacecraft Orbit

Orbit Parameters[30]	
Reference system	Geocentric
Regime	Low Earth, Sun-Synchronous
Launch Date	21 November 2013, 07:11:29 UTC
Perigee	563.8 km
Apogee	592.6 km
Semi-major Axis	6949 km
Inclination	97.7°
Period	96.1 minutes

Table 2: SkySat-1 Orbit Parameters

2.3   Sensors and Actuators

Attitude determination primarily relies on Star Trackers and Inertial Measurement Units with an internal closed-loop control system in charge of running the Attitude Determination and Control scheme. Reaction wheels and magnetic torque rods are the primary actuators of the spacecraft.

SkySat-1 is equipped with two ST-16RT2 star trackers (Sinclair Interplanetary), three TQ-15 magnetic torque rods (built under license by SpaceFlight Industries), and four RW3-1.0 reaction wheels (built under license by Millennium Space Systems).

Star Tracker Parameters[31]	
Accuracy	<7 arcsec RMS cross-boresight, <70 arcsec RMS around boresight
Availability	>99.9%
Size, Mass	59mm x 56mm x 31.5mm, 90g
FOV (Field of View)	7:5° (half axis)
Exposure Time	100 ms
Catalog	3746 stars

Table 3: ST-16 Star Tracker Parameters

Torque Rod Parameters [32]	
Nominal Dipole	15 Am^2 @ 28V
Max Dipole	19 Am^2 @ 34V
Length	228mm
Mass	400g
Resistance	250 Ω nominal each coil

Table 4: TQ-15 Magnetic Torque Rod Parameters

Reaction Wheel Parameters [33]	
Momentum	1.0 Nm-sec @ 6000 rpm
Torque	100 mNm
Power	24V to 34 V

Table 5: RW3-1.0 Reaction Wheel Parameters

2.4   ADCS Requirements

Pointing Accuracy: $\pm 0.1°$ [30]
Slew Rate: 10 deg/s (Estimated from Reaction Wheel Parameters [33])

3   Spacecraft Model

3.1   Model Parameters

The following vehicle parameters were used to create the subsequent vehicle model proposed in this section.

Spacecraft Parameters [30]	
Mass	83 kg
Bus Size	60cm x 60cm x 80cm
Power	120 W OAP (Orbit Average Power)
Attitude Control Accuracy	$\pm 0.1°$
RF Communications	X-band downlink of payload data: 470 Mbit/s
	S-band uplink: 16 kbit/s
	Onboard data storage capacity: 768 GB
Design Life	4 years

Table 6: SkySat-1 Spacecraft Parameters

In order to make a CAD model of this vehicle, emphasis is placed on guaranteeing that the model matches SkySat-1's mass and bus size dimensions. The other parameters will be used primarily in ADCS calculations.

3.2   Vehicle CAD Model

The following model was created in SolidWorks 2017 with an arbitrary body axis as shown below:

(a) Body Frame Axes   (b) Vehicle Model
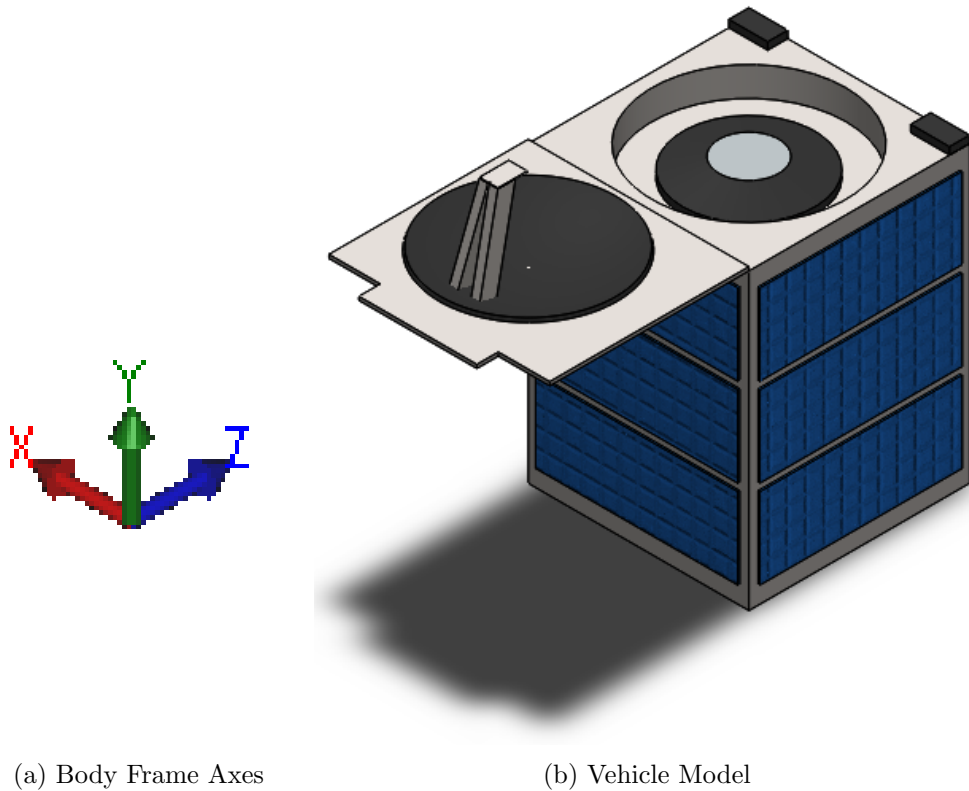
Figure 1: Vehicle Model With Body Axes

To simplify the model, the vehicle was broken down into simple shapes like rectangular prisms, cylinders, and spheres, and held to an assumption that each piece has a uniform density. This simplified model is then used to calculate the vehicle's center of mass and body-frame inertia matrix.

It can be seen from the following figure that the internal components of the satellite were ignored and the internal structure was replaced by a solid body. This assumption was made for two reasons: (1) since the internal structure of the satellite is unknown to the public, and (2) the rectangular prism design of the bus allows its center of mass to only have small asymmetric deviations in center of mass from the true vehicle design (the shape provides a constraint on where the mass-center of the vehicle must be).

(a) Vehicle External Model   (b) Vehicle Internal Model
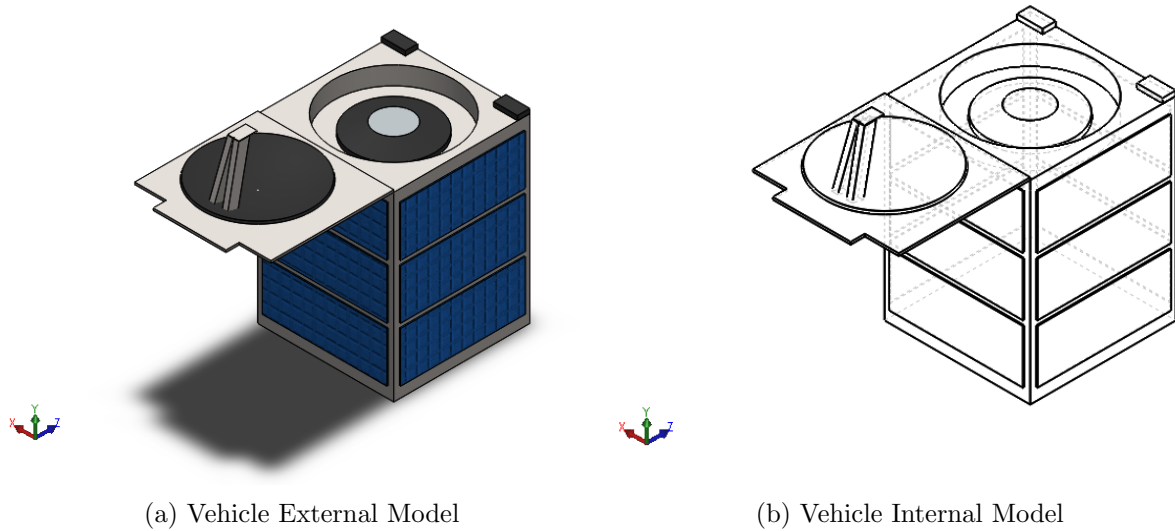
Figure 2: Vehicle Model Used for Mass Property Analysis

3.3   Model Inertia Matrix

From an analysis of the CAD model in SolidWorks 2017, the following mass properties were generated:

Model Parameters	
Mass	83.00 kg
Volume	0.29 m^3
Surface area	4.11 m^2
Center of mass (wrt origin)	X = 0.00 (m) Y = 0.39 Z = -0.01
Principal axes of inertia	$\begin{bmatrix} I_x \\ I_y \\ I_z \end{bmatrix} = \begin{bmatrix} 0.00 & 0.95 & -0.33 \\ 0.00 & -0.33 & 0.95 \\ 1.00 & 0.00 & 0.00 \end{bmatrix}$
Principal moments of inertia	P$_x$ = 5.61 (kg-m^2) P$_y$ = 7.03 P$_z$ = 7.49
Moments of inertia	$\begin{bmatrix} L_x \\ L_y \\ L_z \end{bmatrix} = \begin{bmatrix} 7.49 & 0.00 & 0.00 \\ 0.00 & 5.76 & -0.44 \\ 0.00 & -0.44 & 6.88 \end{bmatrix}$
Moments of inertia	$\begin{bmatrix} I_x \\ I_y \\ I_z \end{bmatrix} = \begin{bmatrix} 20.22 & 0.00 & 0.00 \\ 0.00 & 5.77 & -0.83 \\ 0.00 & -0.83 & 19.60 \end{bmatrix}$

Table 7: CAD Model Parameters

From the information found in the previous table, it can be seen that the rotation matrix corresponding to a transformation from the body frame to the principal frame can be written as:

$$
{}^{b}R^{P} = \begin{bmatrix} I_x \\ I_y \\ I_z \end{bmatrix} = \begin{bmatrix} 0.00 & 0.95 & -0.33 \\ 0.00 & -0.33 & 0.95 \\ 1.00 & 0.00 & 0.00 \end{bmatrix}
$$

3.4 Model Normals

With a discretization of the outer surfaces of the model into simpler planar sections, the following model was generated:
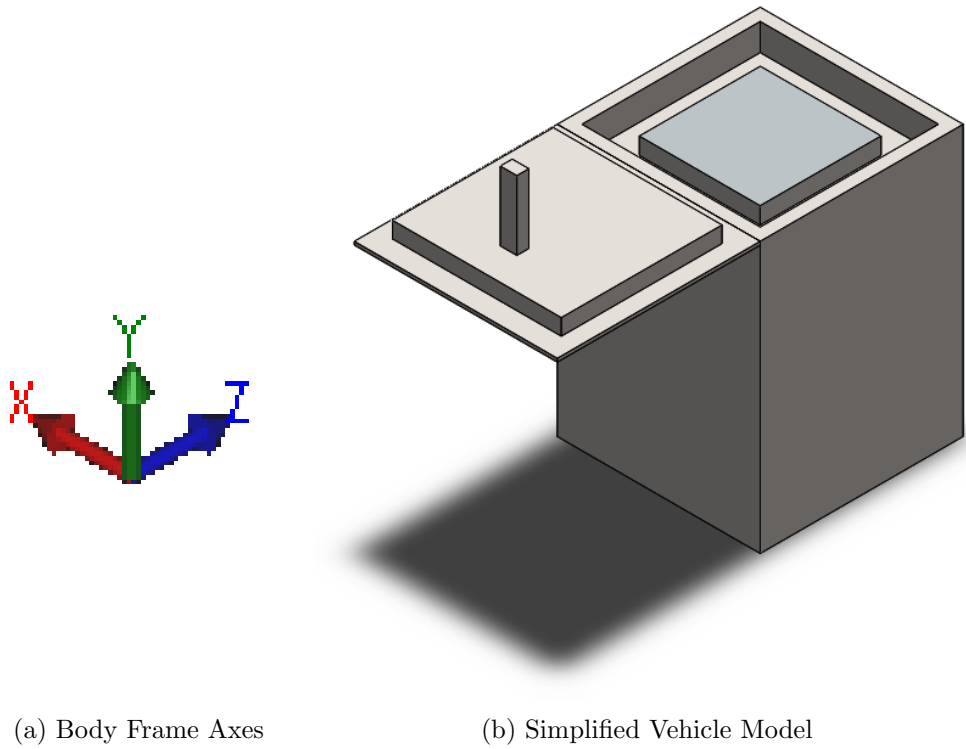
(a) Body Frame Axes   (b) Simplified Vehicle Model

Figure 3: Simplified Vehicle Model With Body Axes

Since this model is entirely composed of rectangular prisms, it is a suitable model to specify the centroid, normal vector, and area of each piece. This will eventually be used to calculate environmental torques such as those due to atmospheric drag.

From a Section Properties analysis of the simplified CAD model, geometric properties were calculated and collected by shared normal vectors. The following information summarizes the simplified model normals analysis:

Model Section Parameters		
Normal Vector	Area	Centroid (wrt c.m.)
$\hat{x}$	0.58m^2	X = -0.25 (m) Y = 0.07 Z = -0.03
$-\hat{x}$	0.58m^2	X = -0.25 (m) Y = 0.07 Z = -0.03
$\hat{y}$	0.96m^2	X = 0.00 (m) Y = 0.41 Z = -0.36
$-\hat{y}$	0.72m^2	X = 0.00 (m) Y = 0.01 Z = -0.29
$\hat{z}$	0.57m^2	X = 0.00 (m) Y = 0.07 Z = 0.22
$-\hat{z}$	0.58m^2	X = 0.00 (m) Y = 0.08 Z = -0.28

Table 8: Simplified Model Normal Vector Section Parameters

4 Dynamics

The following orbit simulations were conducted on Skybox Imaging's SkySat-1 with analysis conducted both with and without Earth Oblateness effects as a function of J_2. All initial conditions were derived from the Two Line Element set (TLE) in Appendix A.

4.1 Keplerian Initial Conditions

The initial conditions of the simulation are provided as a set of Keplerian orbital elements and an initial epoch date and time. Since a TLE for this mission is available, initial launch time is replaced with an active epoch time.

Therefore, although the mission has a launch date of 21 November 2013, 07:11:29 UTC, all initial conditions are taken from the TLE at Epoch: 23 April 2018, 18:27:02 UTC.

$a = 6949.20$ km
$e = 0.0021$
$i = 97.6738°$
$\Omega = 197.6475°$
$\omega = 323.6251°$
$M_0 = 36.3572°$

4.2   Inertial Position and Velocity I.C.'s

By treating these initial Keplerian elements as osculating quantities, computing the corresponding initial position and velocity in the appropriate inertial frame (Earth-Centered Inertial for an Earth-orbiting mission), leads to the following vectors:

$r_0{}^{ECI} = [\,-6611.700,\ -2101.292,\ 14.831\,]'$ [km]
$v_0{}^{ECI} = [\,-0.300,\ 0.967,\ 7.518\,]'$ [km/s]

4.3   Unperturbed Orbit Propagation

For an unperturbed system, vehicle dynamics follow a simple second-order non-linear ODE with zero disturbance forces present. This ODE represents the gravitational acceleration felt on the vehicle in ideal conditions. Using the initial inertial states as provided in section 3.2, the following equation can be numerically integrated [34]:

$$\ddot{\mathbf{r}} + \frac{\mu \mathbf{r}}{r^3} = \mathbf{0}$$

By neglecting any perturbations beyond the two-body spherical gravity force acting on the orbit, the following orbit path was produced over a span of 500 complete orbits with a numerical integration step size of 10 seconds using ode45 numerical integration in Matlab.
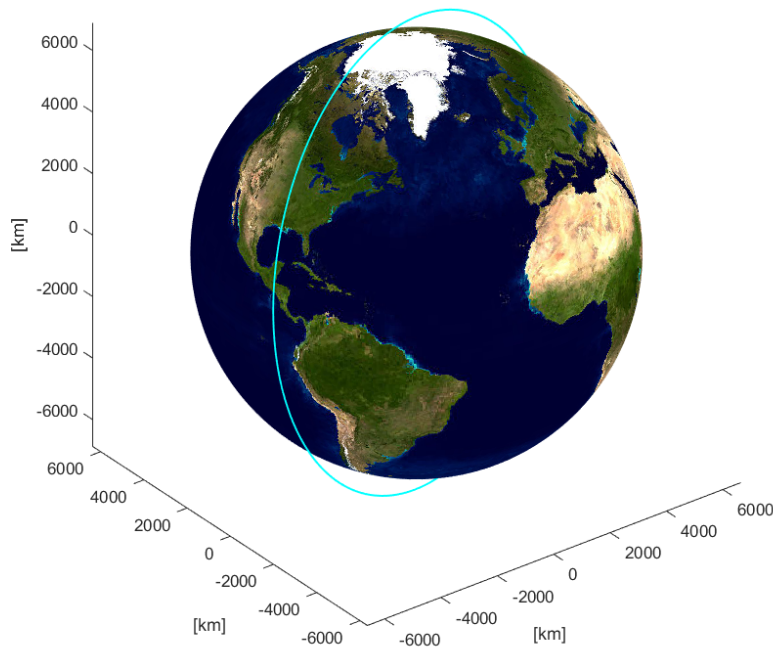

Figure 4: Unperturbed Orbit Path

4.4 Orbit Propagation with J_2 Effects

By considering J_2 effects from Earth oblateness, small disturbances can be introduced into the numerical integration to produce a non-constant orbit path. The governing dynamics then introduce non-zero forces proportional to J_2 as prescribed below [34]:

$$\ddot{X} = -\frac{\mu X}{r^3}\left[1 - \frac{3}{2}J_2\left(\frac{R_e}{r}\right)^2\left(5\frac{Z^2}{r^2} - 1\right)\right]$$

$$\ddot{Y} = -\frac{\mu Y}{r^3}\left[1 - \frac{3}{2}J_2\left(\frac{R_e}{r}\right)^2\left(5\frac{Z^2}{r^2} - 1\right)\right]$$

$$\ddot{Z} = -\frac{\mu Z}{r^3}\left[1 - \frac{3}{2}J_2\left(\frac{R_e}{r}\right)^2\left(5\frac{Z^2}{r^2} - 3\right)\right]$$

The following orbit path was run over the same parameters as Figure 1 with the addition of J_2 effects.

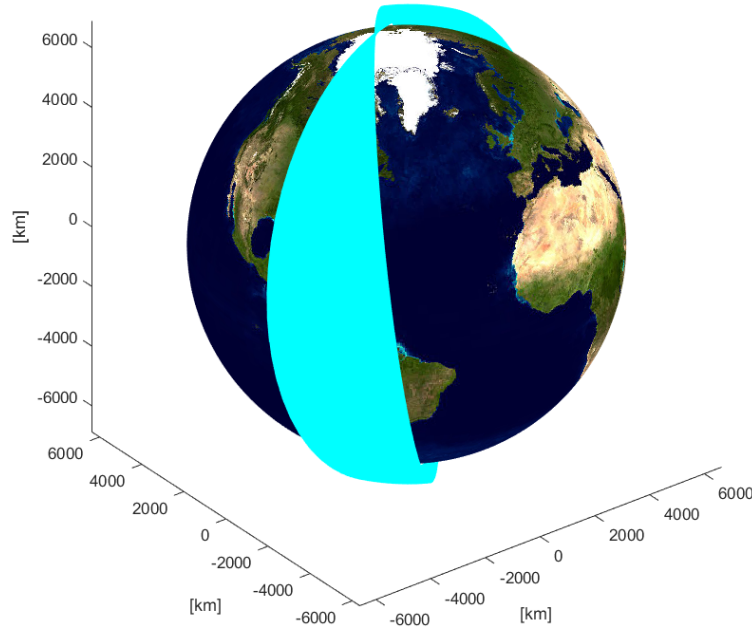Figure 5: Orbit Path with J_2 Perturbation

5 External Torque Dynamics

To increase the realism of the previously demonstrated spacecraft dynamics model, gravity gradient torque and atmospheric drag has been added to the model. Since the orbit of Skysat-1 is placed in LEO, atmospheric drag contribution would significantly outweigh solar radiation pressure, and therefore, solar effects have been neglected.

The following analysis represents a single day (15 orbits) at an integration time step of three seconds:

1. The maximum magnitude of atmospheric drag and gravity gradient torque:

Maximum Atmospheric Drag Torque = 6.8693e-05 N-m
Maximum Gravity Gradient Torque = 2.6296e-08 N-m

2. Over the course of one day (15 orbits), the following plots of altitude decay, angular velocity, and quaternion have been plotted over orbit number:
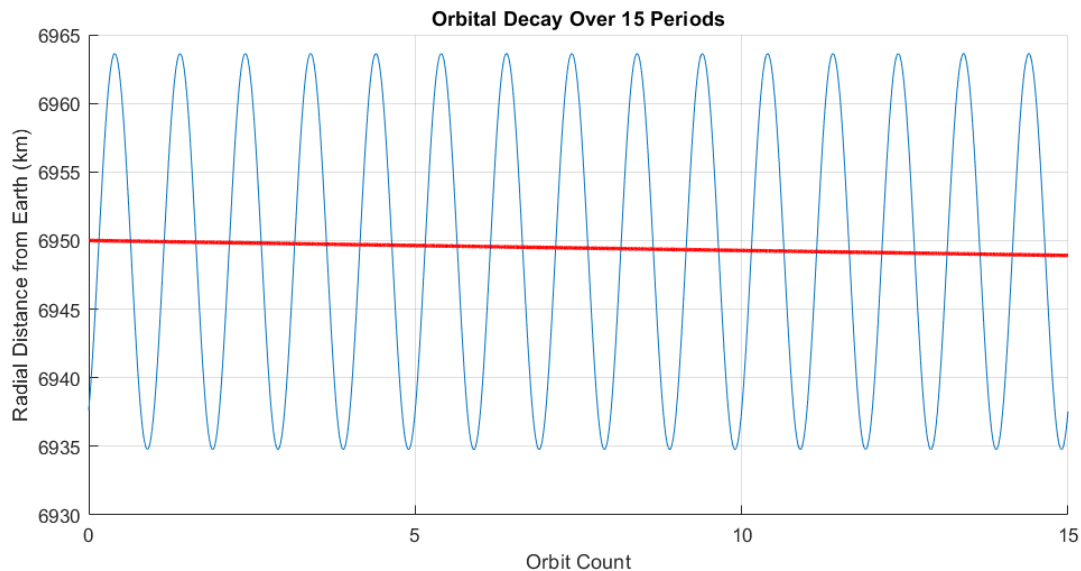
Figure 6: Orbit Altitude vs Period Count

While hard to detect by eye, the orbit decay over a single day is approximately 1.088 kilometers per day (as plotted by the mean semi-major-axis in red). This is to be expected, since anything more would require the vehicle to be boosted into a higher orbit or suffer from a significantly shorter mission lifetime; the small symmetric profile of the vehicle lends to a relatively low torques from both atmospheric drag and gravity gradient torques.

The following represents the correlated angular momentum magnitude throughout the flight:
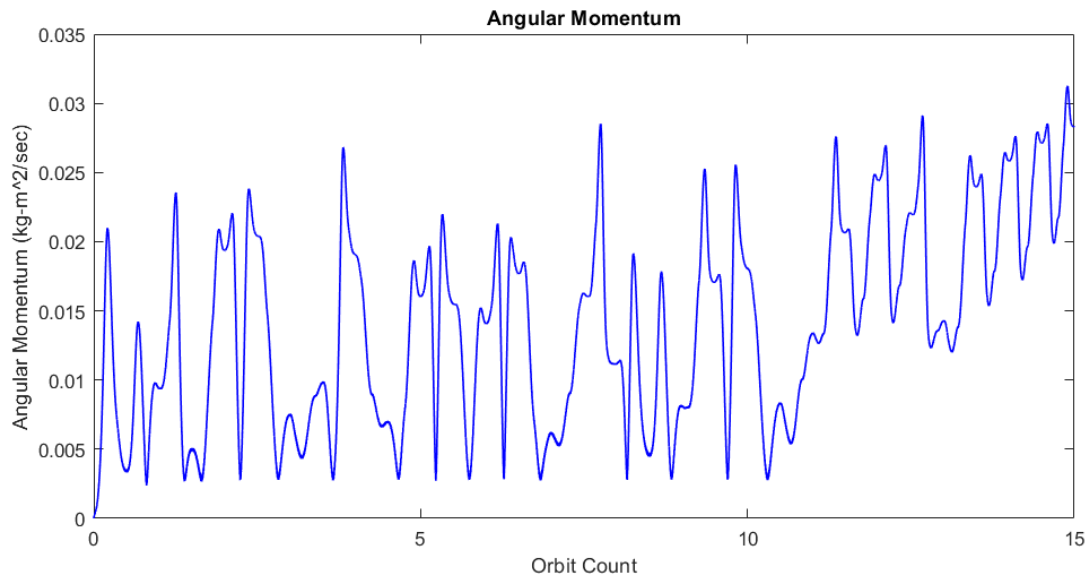
Figure 7: Angular Momentum Vector vs Orbit Count

By starting the vehicle with no spin, the vehicle is placed into a spin around the major axis of the spacecraft with periodic and secular drift from perturbations from external torque (as to be expected). The maximum magnitude of angular velocity to expect over the course of a single day, according to the data producing the plot of angular velocity vector vs orbit count reveals a max of 0.0034 rad/s.

The corresponding quaternion response can be seen in the following plot along the same orbit count:

Figure 8: Quaternion Vector vs Period Count

In general, these results bode quite well for the actuators outlined in the previous part of this section of the report, as the magnitudes of the changes in angular momentum and expected maximum torque are well within the range of actuation by the momentum wheels and magnetic torque rods, and the need for corrections and momentum dumping can be held to a minimum.
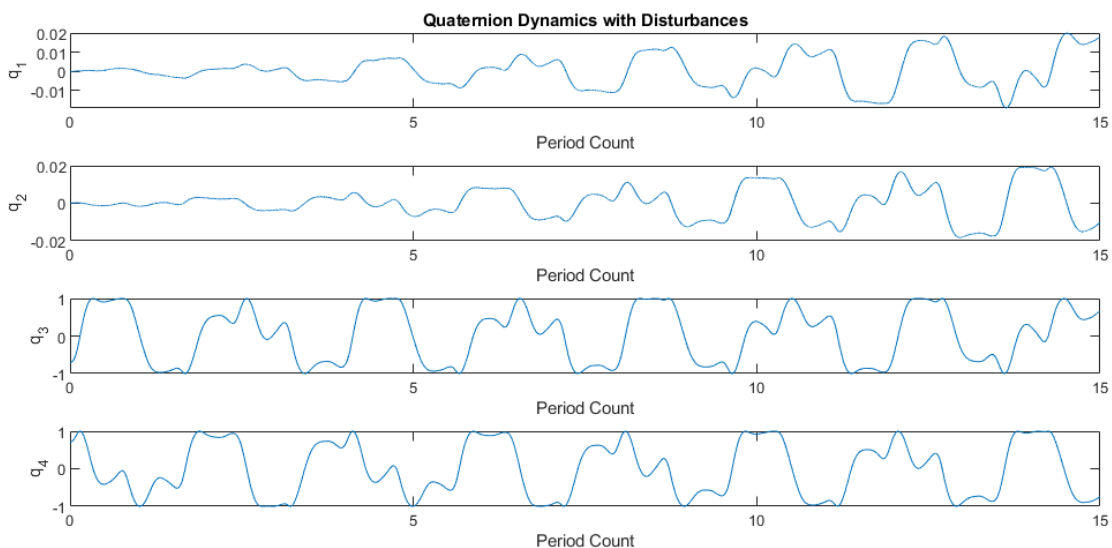
This data, and more particularly the lack of appearance of secular drift, can be easily understood by realizing the low profile of the video keeps disturbance effects to a minimum, despite being in low earth orbit. This incidental benefit of having such a small normal surface area benefits the vehicle not only in weight, but allows the vehicle to operate with low-torque actuators with extreme efficiency.

6   Inertial Stability

6.1   Principal Axis Stability

By implementing Euler's equation using the inertia matrix (see 'Principal moments of inertia' in Table 7), it is possible to verify the the stability of rotation around the principal axes. With an initial condition of $\|w\| = 10$ RPM around the major axis, the scalar value of angular momentum may be calculated. Since angular momentum magnitude is a constant, spin perturbations and axis changes may be simulated by scaling the appropriate components of angular velocity.

By perturbing the angular velocity vector around the three principal axes of the vehicle and propagating the nutation into a series of nutated angular momentum vectors with constant magnitude, the following trajectories may be plotted on a 3D momentum sphere:
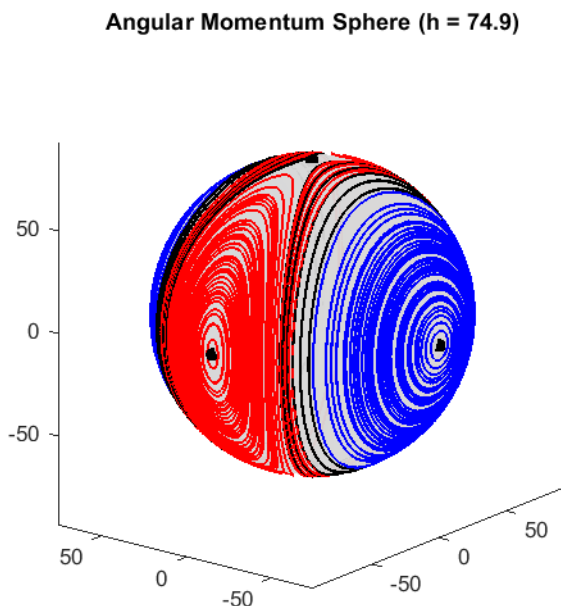

Figure 9: Perturbed Momentum Sphere Trajectories

As seen in the previous figure, not all three axes are stable in the presence of perturbations. While the major axis (blue) is always stable in the range of perturbed motion, and the intermediate axis (black) is always unstable, the minor axis (red) can become unstable in the presence of perturbations.

While it is reasonable to assume a vehicle will most naturally rotate around its major axis, it may become necessary to rotate around an alternate axis for pointing/sensor requirements. Therefore, the use of rotors to spin-stabilize a satellite changes the natural stability of the principal axes, allowing for non-major axes to be artificially supported to have an effective inertia higher than that of the major axis.

6.2   Spin Stabilization

Most modern spacecraft have a "safe mode" built into their operating software that is triggered in the event of a system malfunction. Attitude is an important part of this, as solar panels must be illuminated and communication antennas must be pointed to Earth to keep the spacecraft alive.

Often, a spacecraft is put into a passively stable spin. Design a stable spin configuration for your satellite that keeps the solar panels pointed in an inertially fixed direction (i.e. towards the sun).

In the scope of this project, the normal vector pointing in the $-y$ direction was selected as the safe-mode orientation due to pointing requirements for the primary antenna mounted on the top of the bus.

By implementing an additional rotor in the $-y$ direction, the vehicle may be spin stabilized. Using superspin and dynamic balance requirements, the rotor momentum necessary to stabilize the system was calculated with the constraint that the effective inertia ratio was at least 1.2x the minimum energy axis.

By implementing the gyrostat dynamics into the Euler equation analysis from earlier, a new set of perturbed momentum trajectories can be produced to show stability of the stabilized axis. Since the $-y$-direction exists as the intermediate axis of the vehicle, it should be easy to verify stability via a plot of the momentum sphere:
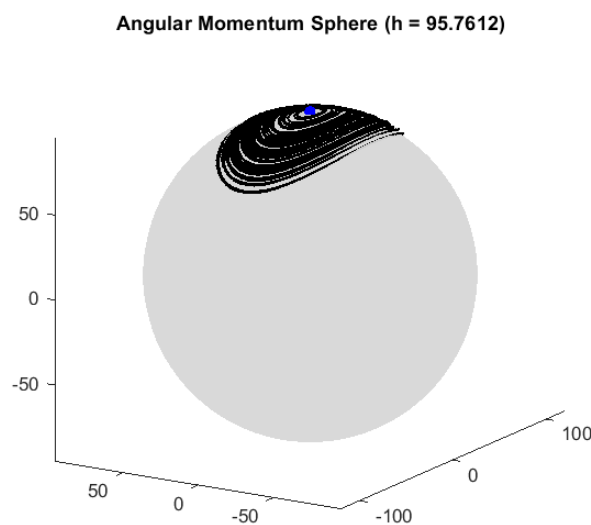

Figure 10: Perturbed Superspin Momentum Sphere Trajectories

By comparing both momentum sphere plots, two features are of note: (1) by adding a specified rotor momentum to the system, the radius of the momentum sphere has grown to compensate for the additional influence of the rotor's axial spin, and (2) the instability of the intermediate axis has been stabilized around an unstable equilibrium with the addition of the superspin and dynamic balance criteria.

6.3   Pointing Accuracy

By adding the gyrostat dynamics to the orbit propagator used earlier in this report, the state vector was augmented to include the attitude quaternion, angular velocity, and rotor momentum in addition to position and velocity.

Simulating the full spacecraft dynamics using the same orbit as last time and the perturbed initial conditions from the previous section, the following components from the attitude quaternion were calculated over a span of 10 seconds to capture several nutation periods:
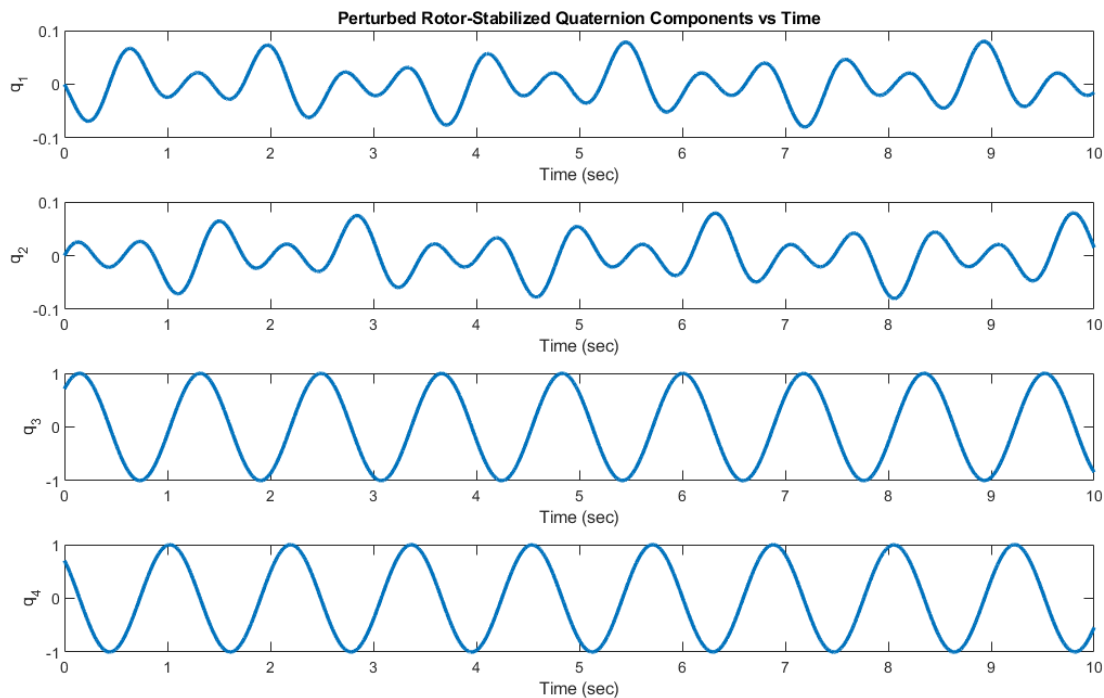

Figure 11: Perturbed Spin-Stabilized Quaternion Vector

For the computation of the pointing error to the -y-axis during the flight of the simulation, the following plot was developed by converting the quaternion into an axis-angle error representation in comparison to the -y-axis orientation.
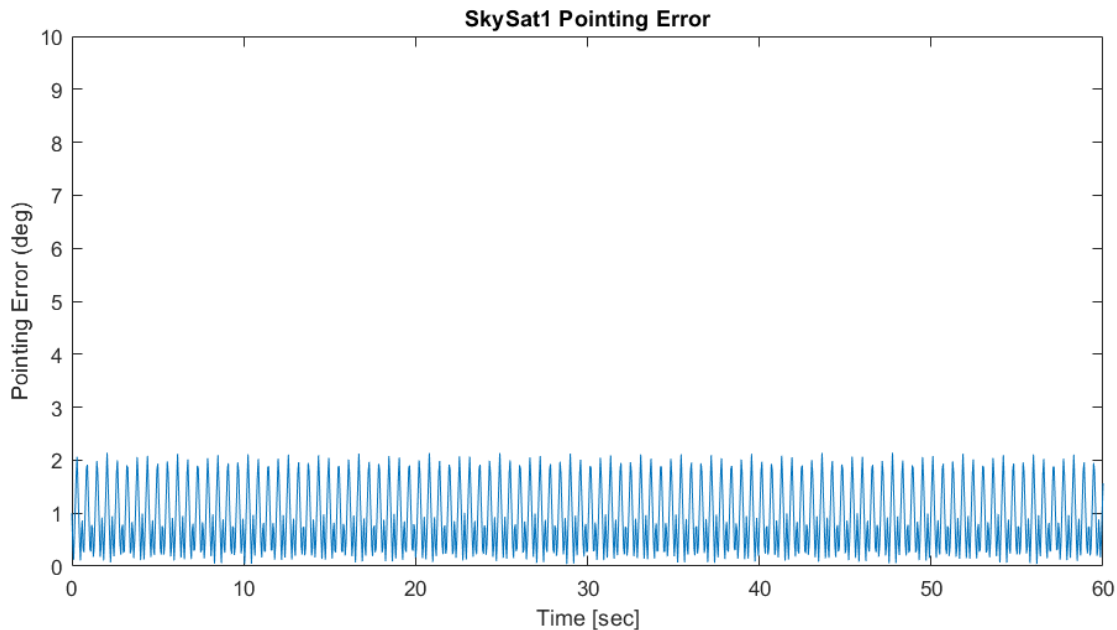
Figure 12: Pointing Accuracy Error over 60 Seconds

As it can be easily discerned from the plot, the gyrostat dynamics stabilize a spin to a maximum of two degrees of error from the -y-axis.

7   Attitude Estimation

7.1   Attitude Sensors

While the SkySat-1 satellite has several onboard attitude sensors such as inertial measurement units and star-trackers, not much information is available on the accuracy of the sensors or which specific methods are embedded into the deployed spacecraft. Therefore, similar/representative sensors will be used from literature.

For the sake of an analysis of attitude determination, a GPS sensor and magnetometer will be used to estimate vehicle state, and a combination of star tracker and gyroscope sensors will be used for the MEKF.

Star Tracker Measurement Error $= diag\,[0.01, 0.02, 0.05]$ (deg)

Gyroscope Rate Noise Density $= 0.018$ (deg/s/sqrt(Hz))
Gyroscope Angular Random Walk $= ARW = 0.002$ (deg/sqrt(Hr))
Gyroscope Covariance $= ARW^2 I(3)$;

GPS Error $= 0.02$ (deg)
Magnetometer Error $= 4.0$ (deg)

NOTE: These values are in need of tuning for more accurate results.

7.2   Static Attitude Estimation

By creating three random orthonormal vectors in the inertial frame and propagating subsequent body frame vectors via the discretized quaternion at each timestep in a six-second orbit simulation. Using the TRIAD, SVD, and Davenport q-Method estimation methods, the following results show a single trial of a Monte Carlo representing the error of the simulation from the true quaternion:
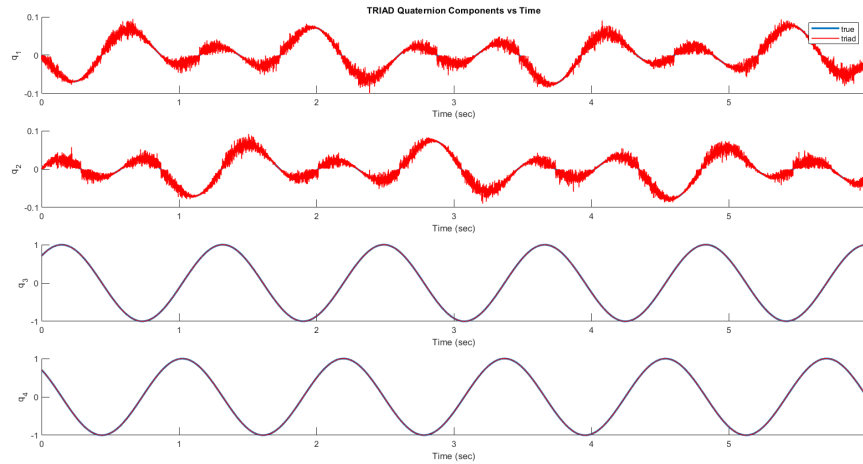
Figure 13: TRIAD Estimated Quaternion Vector
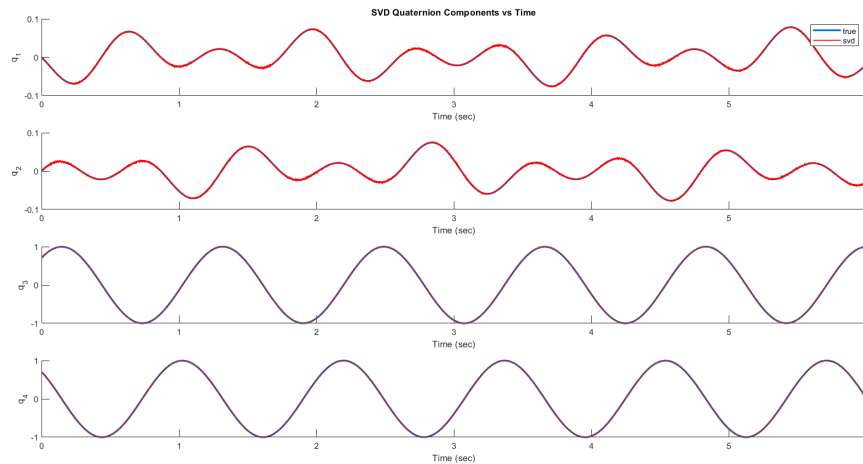
Figure 14: SVD Estimated Quaternion Vector
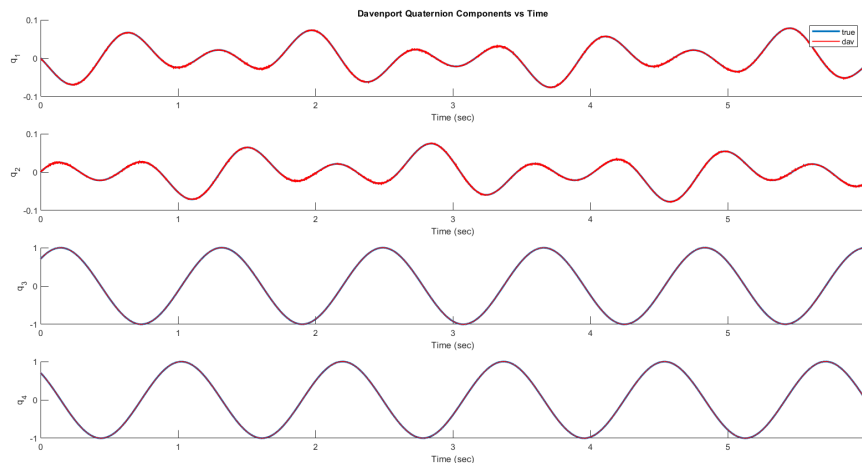
Figure 15: Davenport q-Method Estimated Quaternion Vector

From these plots, discrete error may be calculated (shown in the following figure in degrees) for each method to compare the validity of the method used:
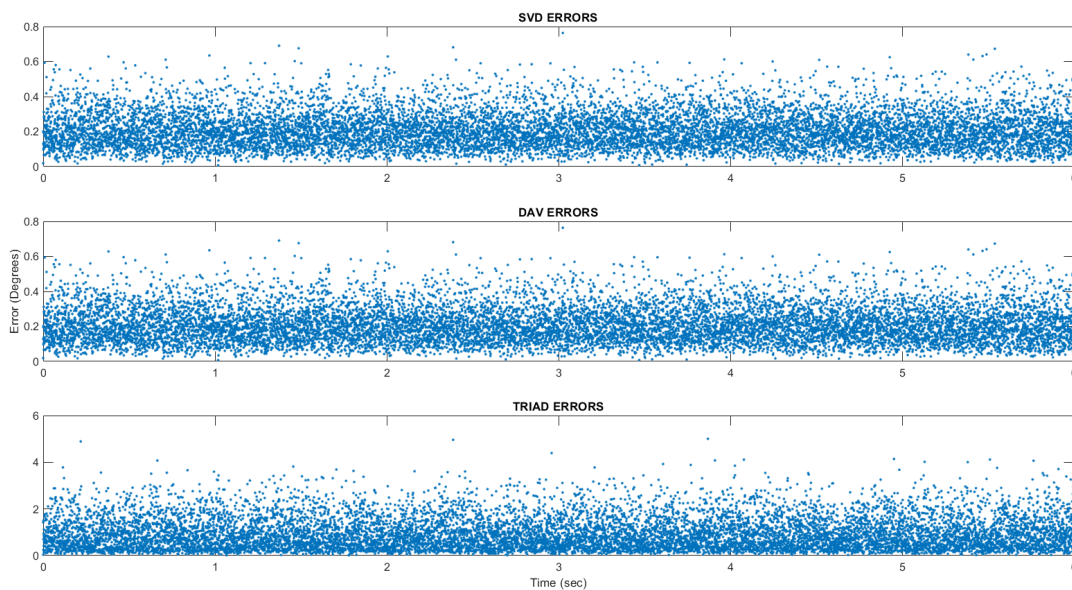
Figure 16: Time-Dependent Static Estimation Method Error

By averaging the results of each method over the orbit propagation and running a series of 2500 trials, the following Monte Carlo simulation of error was produced:
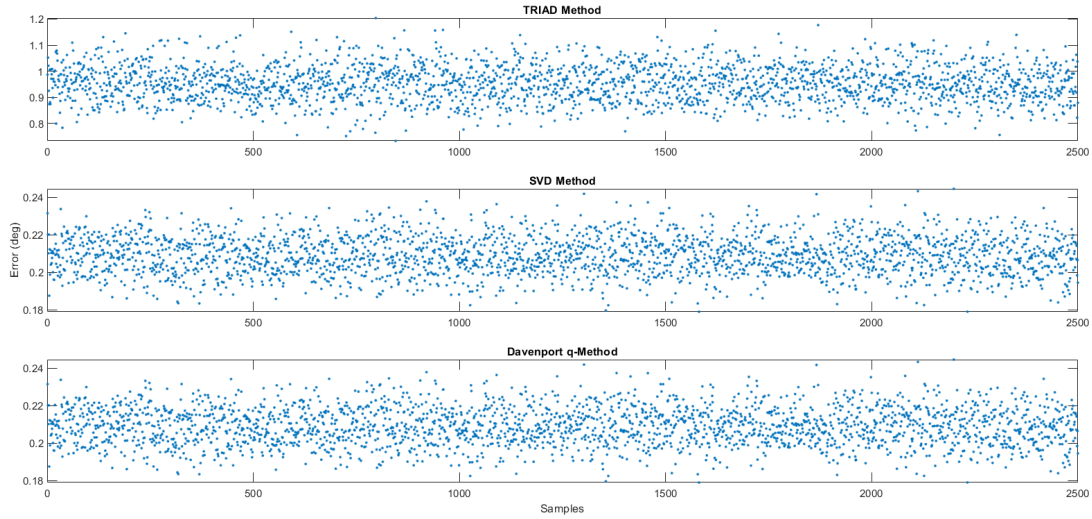
Figure 17: Monte Carlo Simulation of Estimation Methods

From the results of the Monte Carlo directly, the average error from the TRIAD method was 0.9538 °, and from both SVD and Davenport methods was 0.2089 °. As expected, static estimation was proven to be much more accurate using both SVD and Davenport q-Method than TRIAD.

7.3 Recursive Attitude Estimation

7.3.1 MEKF Estimation

In order to implement recursive attitude estimation, an MEKF was implemented to determine vehicle state during the same propagated orbit.

In order to sufficiently sample the data for the MEKF, a sampling rate of 100 Hz was selected for sensor sampling.

The following plots show the results from the implemented MEKF without the addition of star tracker quaternion estimates:

Figure 18: Recursive MEKF Estimated Quaternion
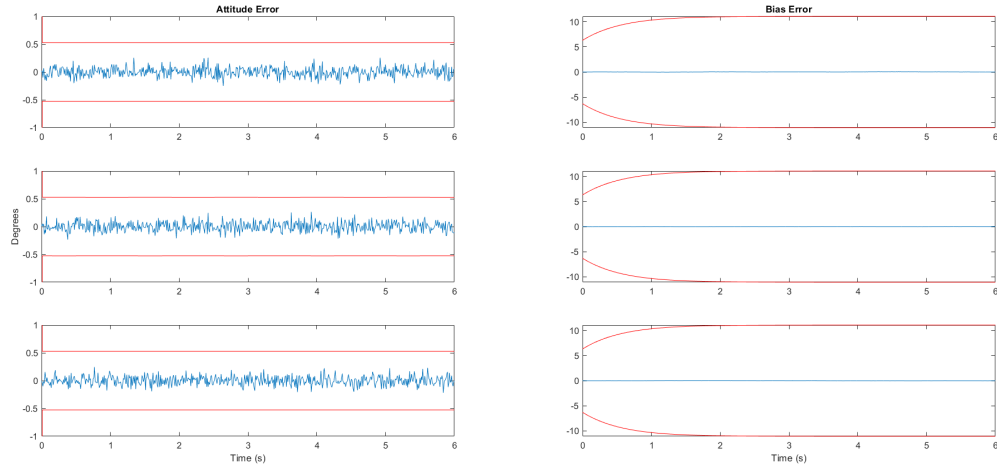
(a) MEKF Axis-Angle Error

(b) MEKF Bias Error

Figure 19: MEKF Error Results

Surprisingly, the results from the MEKF show that the recursive attitude determination method performed better than TRIAD method, but not as well as both Davenport and SVD methods. This may be a result of a lack of additional sensor measurements (i.e. star trackers), or a misalignment of sample rates, leading to overly-noise integration of random walks.

As seen in the MEKF Axis-Angle Error plot, however, it is seen that the attitude error is bounded without the covariance of the sensors, and is therefore a valid estimation of state within the prescribed errors.

In terms of convergence, the filter converges within the bounds of the covariance rapidly, but not without error. While bias error converges to almost zero error, attitude remains bounded, yet noisy. This behavior will be studied in further detail as the project progresses.

7.3.2 Unscented Kalman Filter Estimation

As the chosen expansion of the project outside of the prescribed material, an Unscented Kalman Filter which takes gyroscope inputs and filters quaternion and gyro-bias was implemented on the same parameters as the MEKF.

Since the UKF does not require the linear mapping of the Jacobians, and instead requires the propagation of a set of sigma-points, the filter should do a better job of mapping the non-linearities of the state input vectors. The following algorithm outlines the model implemented in the scope of this paper:

For $k = 1, \ldots, \infty$:

1. Set $t = k - 1$
2. Calculate sigma-points:
$$\boldsymbol{\mathcal{X}}_t^a = \left[\begin{array}{ccc} \hat{\mathbf{x}}_t^a & \hat{\mathbf{x}}_t^a + \zeta\sqrt{\mathbf{P}_t^a} & \hat{\mathbf{x}}_t^a - \zeta\sqrt{\mathbf{P}_t^a} \end{array} \right]$$
3. Time-update equations:
$$\begin{aligned} \boldsymbol{\mathcal{X}}_{k|t}^x &= \mathbf{f}\left(\boldsymbol{\mathcal{X}}_t^x, \boldsymbol{\mathcal{X}}_t^v, \mathbf{u}_t\right) \\ \hat{\mathbf{x}}_k^- &= \sum_{i=0}^{2L} w_i^m \boldsymbol{\mathcal{X}}_{i,k|t}^x \\ \mathbf{P}_{\mathbf{x}_k}^- &= \sum_{i=0}^{2L}\sum_{j=0}^{2L} w_{ij}^c \left(\boldsymbol{\mathcal{X}}_{i,k|t}^x\right)\left(\boldsymbol{\mathcal{X}}_{j,k|t}^x\right)^T \end{aligned}$$
4. Measurement-update equations:
$$\begin{aligned} \boldsymbol{\mathcal{Y}}_{k|t} &= \mathbf{h}\left(\boldsymbol{\mathcal{X}}_{k|t}^x, \boldsymbol{\mathcal{X}}_t^n\right) \\ \hat{\mathbf{y}}_k^- &= \sum_{i=0}^{2L} w_i^m \boldsymbol{\mathcal{Y}}_{i,k|t} \\ \mathbf{P}_{\tilde{\mathbf{y}}_k} &= \sum_{i=0}^{2L}\sum_{j=0}^{2L} w_{ij}^c \left(\boldsymbol{\mathcal{Y}}_{i,k|t}\right)\left(\boldsymbol{\mathcal{Y}}_{i,k|t}\right)^T \\ \mathbf{P}_{\mathbf{x}_k \mathbf{y}_k} &= \sum_{i=0}^{2L}\sum_{j=0}^{2L} w_{ij}^c \left(\boldsymbol{\mathcal{X}}_{i,k|t}^x\right)\left(\boldsymbol{\mathcal{Y}}_{i,k|t}\right)^T \\ \mathbf{K}_k &= \mathbf{P}_{\mathbf{x}_k \mathbf{y}_k} \mathbf{P}_{\tilde{\mathbf{y}}_k}^{-1} \\ \hat{\mathbf{x}}_k &= \hat{\mathbf{x}}_k^- + \mathbf{K}_k\left(\mathbf{y}_k - \hat{\mathbf{y}}_k^-\right) \\ \mathbf{P}_{\mathbf{x}_k} &= \mathbf{P}_{\mathbf{x}_k}^- - \mathbf{K}_k \mathbf{P}_{\tilde{\mathbf{y}}_k} \mathbf{K}_k^T \end{aligned}$$

where $\hat{x}_k$ represents the estimated state and P_{x_k} represents the estimated covariance at each timestep.

The following plots show the results from the implemented MEKF without the addition of star tracker quaternion estimates for the UKF:
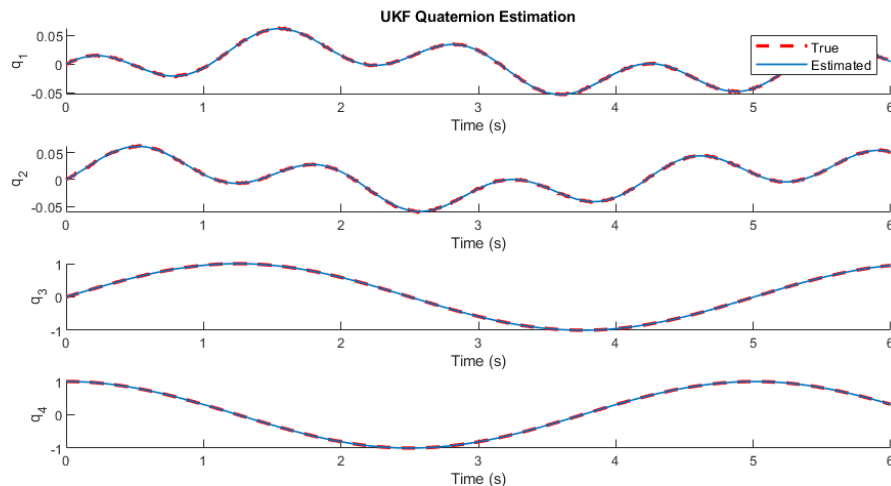
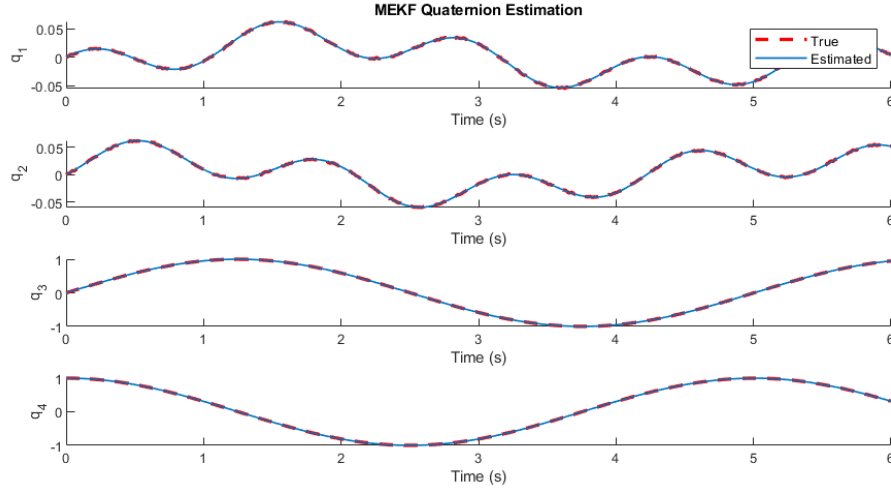Figure 20: Recursive UKF Estimated Quaternion
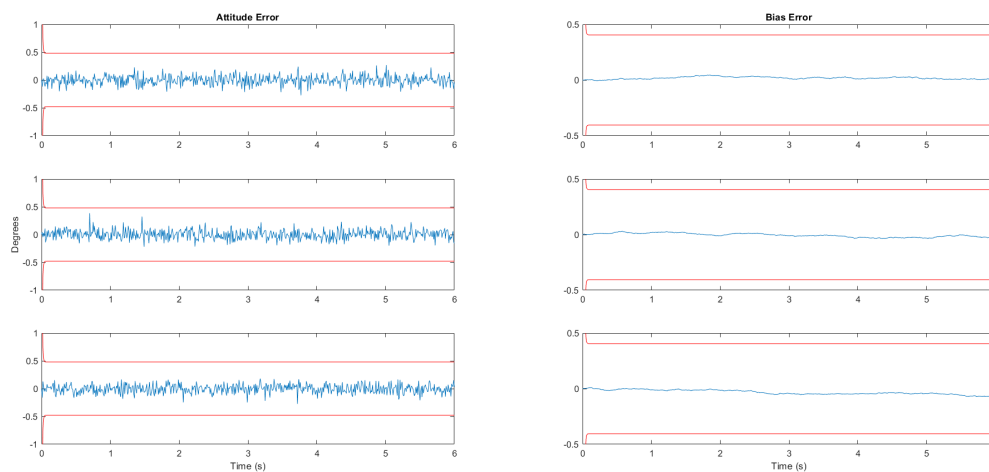
(a) UKF Axis-Angle Error

(b) UKF Bias Error

Figure 21: UKF Error Results

From these results, it is clear to see that both the EKF and UKF perform well under the prescribed initial conditions, and track quaternion state input extraordinarily well. Since the Unscented Transform of the UKF is a better representation of the non-linear system than the EKF, it is expected to see that the error covariances for the UKF are indeed lower than the EKF.

What the UKF does not improve upon, however, is computational efficiency, as the production and propagation of sigma-points and mean-quaternion calculations is computationally taxing on the algorithm.

Table 9: Recursive Estimation Runtime COmparison

EKF	UKF
0.2424 sec	4.6057 sec

From this information, it is easy to see that, although the UKF performed well in estimating the quaternion state of the system, it took 19x longer than the EKF to derive a marginally better result.

8 Attitude Control

As mentioned previously in this report, the vehicle implements a set of RW3-1.0 reaction wheels and TQ-15 magnetic torque rods for the purpose of attitude control. Onboard Skysat-1 are four reaction wheels and three torque rods, but specified position and orientation specifications are not available; therefore, estimations have been used to justify both position and alignment of the actuators aboard the spacecraft.

8.1 Actuator Parameters

The following outlines the specified parameters used for the subsequent orbital dynamics analysis:

8.1.1 Reaction Wheels

The maximum torque and maximum angular momentum:

Reaction Wheel Parameters [33]	
Momentum	1.0 Nm-sec @ 6000 rpm
Torque	100 mNm
Power	24V to 34 V

Table 10: RW3-1.0 Reaction Wheel Parameters

Reaction wheel positions and orientations in the spacecraft body frame:

Actuator	Position	Orientation
RW1	$^b[0.25, 0, -0.25]$	$^b[-\frac{1}{\sqrt{3}}, \frac{1}{\sqrt{3}}, \frac{1}{\sqrt{3}}]$
RW2	$^b[0.25, 0, 0.25]$	$^b[-\frac{1}{\sqrt{3}}, \frac{1}{\sqrt{3}}, -\frac{1}{\sqrt{3}}]$
RW3	$^b[-0.25, 0, -0.25]$	$^b[\frac{1}{\sqrt{3}}, \frac{1}{\sqrt{3}}, \frac{1}{\sqrt{3}}]$
RW4	$^b[-0.25, 0, 0.25]$	$^b[\frac{1}{\sqrt{3}}, \frac{1}{\sqrt{3}}, -\frac{1}{\sqrt{3}}]$

Table 11: Reaction Wheel Body Position and Orientation Vectors

Jacobian matrix mapping reaction wheel commands into body-frame torque and momentum:

$$^bJ = \begin{bmatrix} ^ba_1 & ^ba_2 & ^ba_3 & ^ba_4 \end{bmatrix} = \begin{bmatrix} -\frac{1}{\sqrt{3}} & -\frac{1}{\sqrt{3}} & \frac{1}{\sqrt{3}} & \frac{1}{\sqrt{3}} \\ \frac{1}{\sqrt{3}} & \frac{1}{\sqrt{3}} & \frac{1}{\sqrt{3}} & \frac{1}{\sqrt{3}} \\ \frac{1}{\sqrt{3}} & -\frac{1}{\sqrt{3}} & \frac{1}{\sqrt{3}} & -\frac{1}{\sqrt{3}} \end{bmatrix}$$

8.1.2   Magnetic Torque Rods

Maximum torque and maximum angular momentum:

Torque Rod Parameters [32]	
Nominal Dipole	15 Am^2 @ 28V
Max Dipole	19 Am^2 @ 34V
Length	228mm
Mass	400g
Resistance	250 Ω nominal each coil

Table 12: TQ-15 Magnetic Torque Rod Parameters

Torque rod positions and orientations in the spacecraft body frame:

Actuator	Position	Orientation
TR1	^{b}[0.30, 0.30, -0.25]	^{b}[1, 0, 0]
TR2	^{b}[0.30, 0.30, -0.25]	^{b}[0, 1, 0]
TR3	^{b}[0.30, 0.30, -0.25]	^{b}[0, 0, 1]

Table 13: Torque Rods Body Position and Orientation Vectors

Jacobian matrix mapping torque rod commands into body-frame torque and momentum:

$$^bJ = \begin{bmatrix} -^b\hat{B}_1 & -^b\hat{B}_2 & -^b\hat{B}_3 \end{bmatrix}$$

8.2   Attitude Regulation

In order to control the attitude of the SkySat-1 cubesat, a time-invariant LQR control design method was implemented. This controller was integrated with the dynamics of the vehicle so that the input of the controller was the state estimate of the MEKF from the previous analysis.

As input to the LQR algorithm for time-invariant attitude control, the following Q and R matrices were used as input:

$$Q = \begin{bmatrix} 1 & 0 & 0 & 0 & 0 & 0 \\ 0 & 1 & 0 & 0 & 0 & 0 \\ 0 & 0 & 1 & 0 & 0 & 0 \\ 0 & 0 & 0 & 1 & 0 & 0 \\ 0 & 0 & 0 & 0 & 1 & 0 \\ 0 & 0 & 0 & 0 & 0 & 1 \end{bmatrix} \qquad R = \begin{bmatrix} 10^8 & 0 & 0 \\ 0 & 10^8 & 0 \\ 0 & 0 & 10^8 \end{bmatrix}$$

From this, graphs of the resulting behavior of the controller with initial error of 10, 25, 45, and 90 pointing accuracy error, and their subsequent mean pointing error were produced. The consensus from this series is that the behavior of the LQR-Controlled attitude dynamics with disturbances and the MEKF performed extremely well, and was able to reduce total attitude error to within tolerance in under an hour for a wide range of initial conditions.

The following graphs visualize the results of this simulation:

(a) 10° Initial Error (RMS Error = 0.7082°)   (b) 25° Initial Error (RMS Error = 1.7840°)
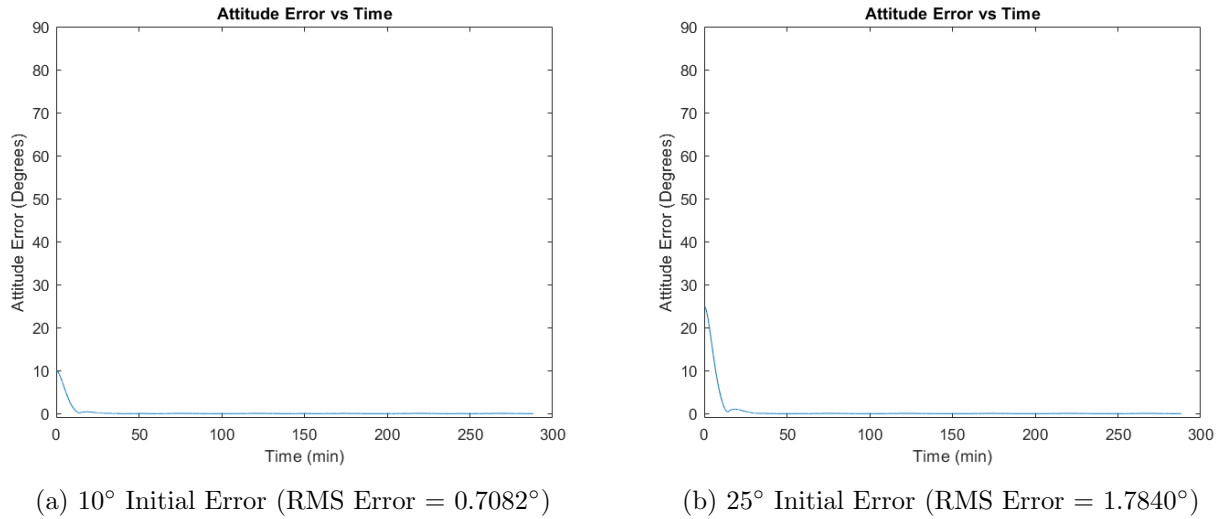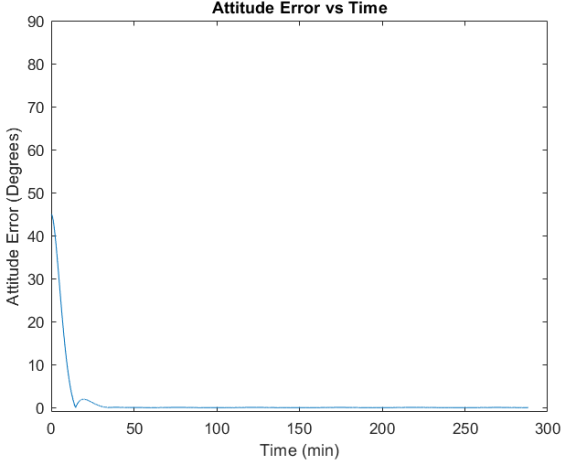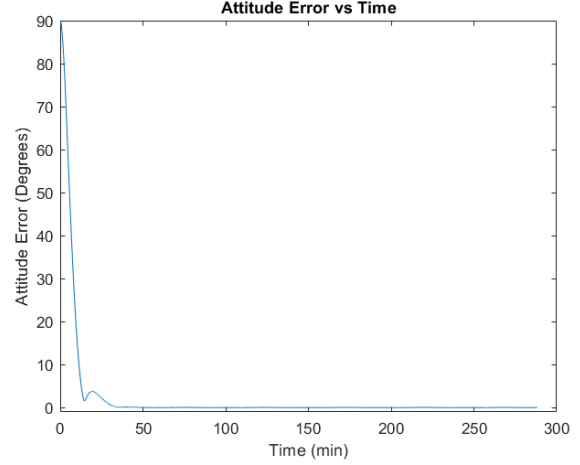
Figure 22: Attitude Error vs Time

(a) 45° Initial Error (RMS Error = 3.3140°)   (b) 90° Initial Error (RMS Error = 6.5607°)

Figure 23: Attitude Error vs Time

8.3 Eigen-Axis Slew

From this time-invariant LQR approach, a time-variant control method was then implemented. This Time-Variant LQR algorithm generates state and input trajectories for an eigen-axis slew maneuver between specified initial and final attitudes with a specified maneuver time using the versine method and inverse dynamics to calculate actuator torques. LQR is used to track the nominal trajectory in the presence of disturbances, which were produced using an RK4 numerical integration. The closed-loop system was then simulated with state estimates from the MEKF and the full spacecraft dynamics.

The following Q and R matrices were used to evaluate the TVLQR algorithm:

$$
Q = \begin{bmatrix}
1 & 0 & 0 & 0 & 0 & 0 & 0 & 0 & 0 \\
0 & 1 & 0 & 0 & 0 & 0 & 0 & 0 & 0 \\
0 & 0 & 1 & 0 & 0 & 0 & 0 & 0 & 0 \\
0 & 0 & 0 & 1 & 0 & 0 & 0 & 0 & 0 \\
0 & 0 & 0 & 0 & 1 & 0 & 0 & 0 & 0 \\
0 & 0 & 0 & 0 & 0 & 1 & 0 & 0 & 0 \\
0 & 0 & 0 & 0 & 0 & 0 & 1 & 0 & 0 \\
0 & 0 & 0 & 0 & 0 & 0 & 0 & 1 & 0 \\
0 & 0 & 0 & 0 & 0 & 0 & 0 & 0 & 1
\end{bmatrix}
\qquad
R = \begin{bmatrix}
100 & 0 & 0 \\
0 & 100 & 0 \\
0 & 0 & 100
\end{bmatrix}
$$

The following is the result of the nominal and closed-loop states and control inputs as given by the Time-Variant LQR algorithm over a 179 degree slew maneuver (to avoid wrapping issues in plotting):
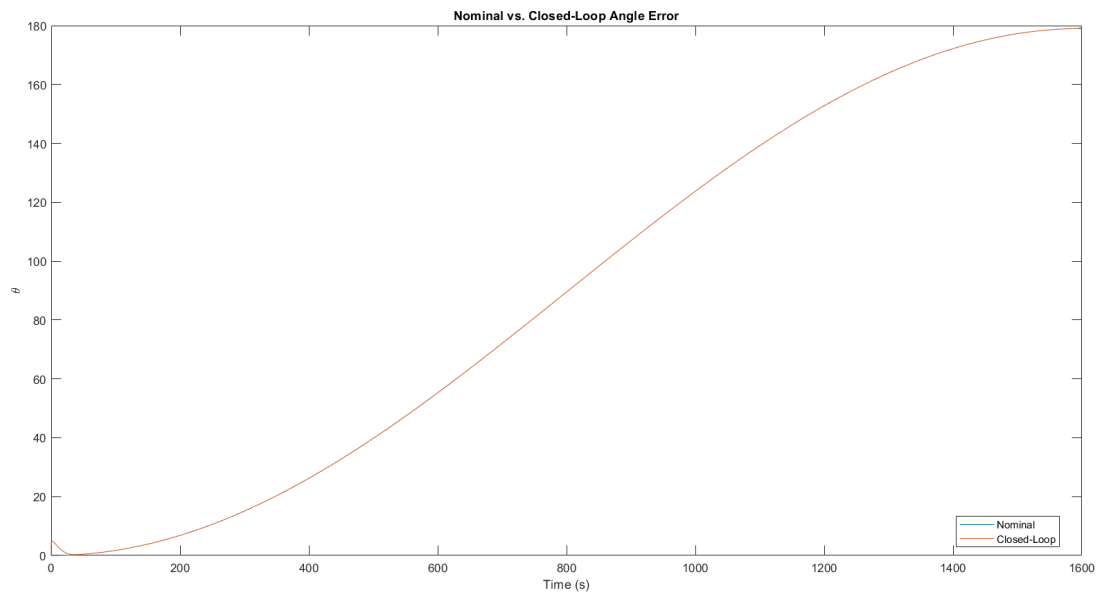
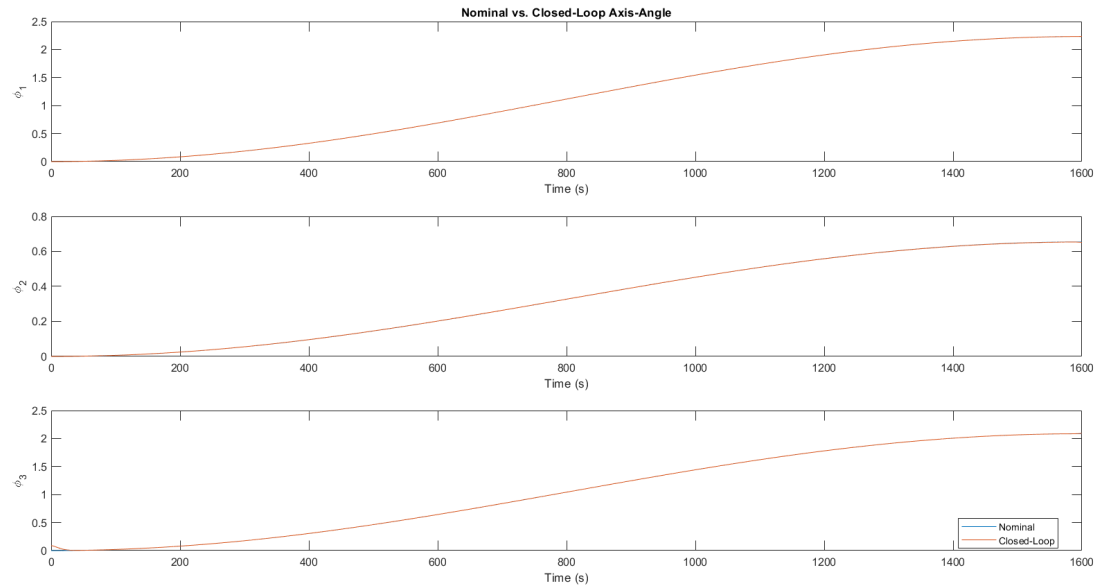Figure 24: Open and Closed-Loop Angle Error vs Time

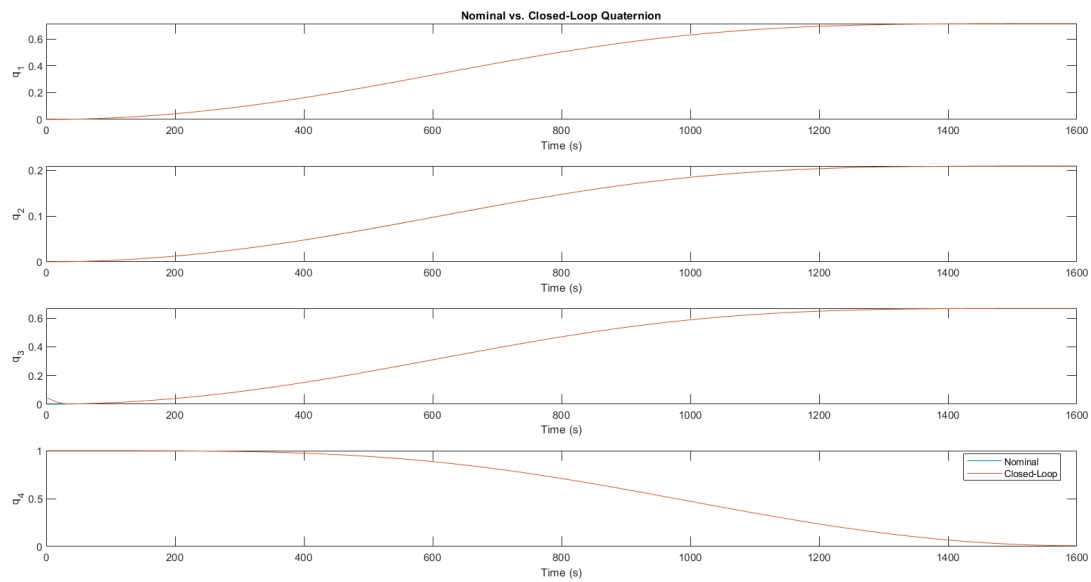Figure 25: Open and Closed-Loop Axis Angle Error vs Time

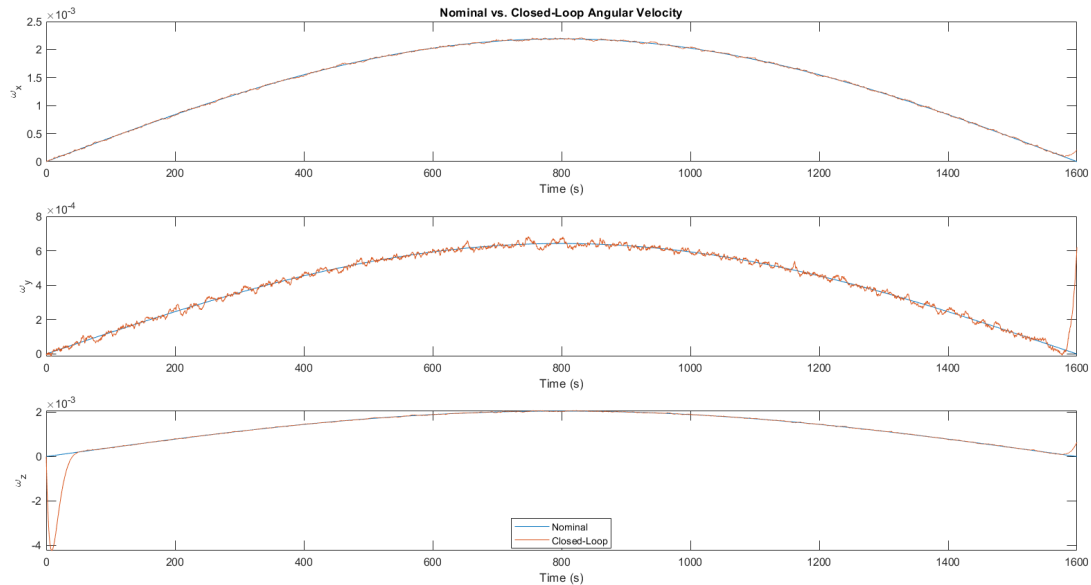Figure 26: Open and Closed-Loop Quaternion vs Time

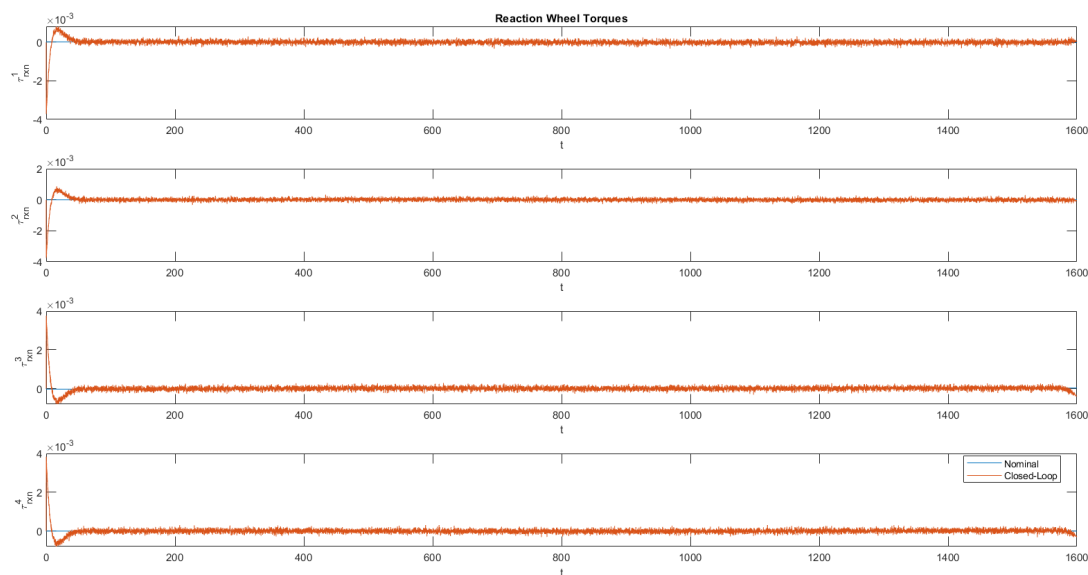Figure 27: Open and Closed-Loop Angular Velocity vs Time

Figure 28: Open and Closed-Loop Control Inputs vs Time

In comparison to the regulator controller, the TVLQR algorithm tracks the eigen-axis slew well, but work may continue to be done to manipulate the Q and R matrices to result in better performance.

9   Conclusion

This report represents the efforts of simulating the ADCS of the SKySat1 Earth-imaging satellite in LEO, subject to nonlinear dynamics, environmental torques, static and recursive state estimation, and both active and passive control mechanisms complete with on-board sensor noise. While this project was a small, fairly simple cubesat, it was clear to see the trade-offs one makes when designing satellites for ADCS purposes. Although its size and weight make it the ideal candidate for inexpensive missions, the lack of powerful control-means requires the vehicle to undergo slow and low-torque reconfigurations. Overall, the simulation of the SkySat1 satellite was a success, as it was proven to be trackable and controllable in the presence of a variety of disturbances.

10   Future Work

As it relates to the mission design of the SkySat program, adapting these satellites to a multi-body simulation that simulates formation-flying would be an obvious next step. Although the domain of formation-flying falls more in line with orbital mechanics than ADCS, implementing pointing requirements for a multi-body system would tie both fields together and expand the project to simulate objective-based missions such as traffic monitoring or intelligence, surveillance, and reconnaissance (ISR) missions.

Appendices

A   Two Line Element Sets (TLE)

```
SKYSAT-1
1 39418U 13066C   18113.76877470  .00000289  00000-0  28950-4 0  9998
2 39418  97.6738 197.6475 0020756 323.6251  36.3572 14.98649985241598
```

B   GitHub Repository URL

https://github.com/cwc5613/SkySat-1-ADCS.git

References

[1] "Terra Bella Officially Joins Planet". planet.com. Retrieved 18 April 2017.

[2] Perry, Tekla S. (1 May 2013). "Start-up Profile: Skybox Imaging". IEEE Spectrum. Retrieved 12 May 2014.

[3] Henry, Caleb (2014-08-05). "Google Closes Skybox Imaging Purchase". Via Satellite. Retrieved 2014-08-10.

[4] Wogan, David (30 December 2013). "High-definition video from space is available for purchase. Finally". Scientific American. Retrieved 12 May 2014.

[5] SkySat-C Generation Satellite Sensors. (n.d.). Retrieved from https://www.satimagingcorp.com/satellite-sensors/skysat-1/

[6] Truong, Alice (11 December 2013). "Proof That Cheaper Satellites Still Can Take Incredibly Detailed Photos of Earth". Fast Company. Retrieved 12 May 2014.

[7] "High-Performance Satellites". Skybox Imaging. Archived from the original on 17 March 2015. Retrieved 17 March 2017.

[8] "Inside a Startup's Plan to Turn a Swarm of DIY Satellites Into an All-Seeing Eye". wired.com. Retrieved 4 November 2017.

[9] "High Resolution Smallsats Built by SSL Arrive at Vandenberg AFB for Launch". sslmda.com (Press release). Space Systems/Loral, LLC. 5 September 2017. Retrieved 1 November 2017.

[10] "REQUEST OF SKYBOX IMAGING, INC. FOR DETERMINATION OF COMPLIANCE WITH SATELLITE IMPLEMENTATION MILESTONES". Federal Communications Commission. 4 March 2013. Retrieved 1 November 2017.

[11] "Planet Doubles Sub-1 Meter Imaging Capacity With Successful Launch Of 6 SkySats". www.planet.com (Press release). Planet Labs Inc.

[12] Henry, Caleb (5 August 2016). "Terra Bella's SkySat 3 Green Propulsion System Declared Operational - Via Satellite -". Via Satellite. Retrieved 1 November 2017.

[13] Clark, Stephen. "Silo-launched Dnepr rocket delivers 32 satellites to space". Website. Spaceflight Now. Retrieved 12 May 2014.

[14] Truong, Alice. "Proof That Cheaper Satellites Still Can Take Incredibly Detailed Photos Of Earth". Website. Fast Company. Retrieved 11 December 2013.

[15] Hearn, Mark. "Skybox Imaging successfully launches its SkySat-2 Earth observation satellite". Website. 9to5Google. Retrieved 8 July 2014.

[16] Eisenberg, Anne (10 August 2013). "Microsatellites: What Big Eyes They Have". The New York Times. Retrieved 12 May 2014.

[17] Henry, Caleb. "Skybox Imaging Releases First Images from SkySat 2". Website. Satellite Today. Retrieved 11 July 2014.

[18] "Skybox Imaging Selects SSL To Build 13 Low Earth Orbit Imaging Satellites". sslmda.com. 10 February 2014. Retrieved 11 August 2016.

[19] "Terra Bella Evaluating Launches for Eight SkySats by 2017". Satellite Today. Access Intelligence. 6 April 2016. Retrieved 11 August 2016.

[20] "SkySat-3 First Light". Terra Bella Blog. Google, Inc. 28 June 2016. Retrieved 11 August 2016.

[21] "International Assortment of Satellites lifted by Indian PSLV Rocket". Spaceflight101.com. 22 June 2016. Retrieved 11 August 2016.

[22] "VIKRAM SARABHAI SPACE CENTRE - PSLV". ISRO. Retrieved 18 April 2015.

[23] "Alphabet Investor Relations". google.com. 9 June 2014. Retrieved 11 August 2016.

[24] "Skybox Imaging + Google". 8 June 2014. Retrieved 29 June 2016.

[25] Lardinois, Frederic (8 March 2016). "Google renames its satellite startup, Skybox Imaging, to Terra Bella and adds focus on image analysis". TechCrunch. AOL Inc. Retrieved 8 March 2016.

[26] Protalinski, Emil (8 March 2016). "Google rebrands Skybox as Terra Bella, will launch 'more than a dozen satellites' over the next few years". VentureBeat. Retrieved 8 March 2016.

[27] Clark, Stephen (16 September 2016). "Vega rocket hauls up quintet of Earth observation satellites". Spaceflight Now.

[28] "Google sells satellite imaging business Terra Bella to Planet Labs". Reuters. 3 February 2017. Retrieved 3 February 2017.

[29] Graham, William (31 October 2017). "Orbital ATK Minotaur-C launches SkySat mission out of Vandenberg". NASASpaceFlight.

[30] Kiran Murthy, Michael Shearn, Byron D. Smiley, Alexandra H. Chau, Josh Levine, Dirk Robinson, " SkySat-1: very high-resolution imagery from a small satellite ", Proceedings of. SPIE , Vol. 9241, 'Sensors, Systems, and Next-Generation Satellites XVIII, Roland Meynart, Steven P. Neeck, Haruhisa Shimoda (editors), Amsterdam, Netherlands, September 22, 2014, 92411E (October 7, 2014); doi:10.1117/12.2074163

[31] Dzamba, John Enright, Doug Sinclair, Kofi Amankwah, Ronny Votel, Ilija Jovanovic, Geoffrey McVittie, "Success by 1000 Improvements: Flight Qualification of the ST-16 Star Tracker," Proceedings of the 28th Annual AIAA/USU Conference on Small Satellites, Logan, Utah, USA, August 2-7, 2014, paper: SSC14-XII-1, URL: http://digitalcommons.usu.edu/smallsat/2014/YearReview/1

[32] Sinclair Interplanetary. (2011). Microsatellite Torque Rods [Brochure]. Author.

[33] Millennium Space Systems. (2017). RWA1000 Small Satellite Reaction Wheel [Brochure]. Author.

[34] K. Alfriend, S. Vadali, P. Gurfil, J. How, and L. Breger, *Spacecraft Formation Flying: Dynamics, Control, and Navigation.* Elsevier Astrodynamics Series, 2010.